Geochimica et Cosmochimica Acta 413 (2026) 204–217

Contents lists available at ScienceDirect

Geochimica et Cosmochimica Acta

journal homepage: www.elsevier.com/locate/gca

Precipitation kinetics and C isotope fractionation of rhodochrosite at 298.15 K

Clancy Zhijian Jiang *, Ziwei Liu, Nicholas J. Tosca

Department of Earth Sciences, University of Cambridge, Downing Street, Cambridge, CB2 3EQ, England, United Kingdom

ARTICLE INFO

Associate editor: Encarnacion Ruiz Agudo

Dataset link: https://doi.org/10.17632/87ykcvn58x.1

Keywords:
Rhodochrosite
Precipitation kinetics
Kinetic isotope effect
Manganese
Aqueous geochemistry

ABSTRACT

Before the rise of atmospheric oxygen, the release and transport of soluble manganese (Mn^{2+}) represented the entry point of the earliest Mn cycle. The Mn cycle on early Earth is thought to have resembled that of Fe due to their geochemical similarities. However, kinetic data pertaining to Mn(II) mineralisation are lacking, and thus we lack a complete understanding of the fate of Mn^{2+} in aqueous systems on early Earth. This study investigates Mn mineralisation and precipitation kinetics through three processes at room temperature: (1) the homogeneous nucleation of rhodochrosite ($MnCO_3$) from oversaturated solutions, (2) seeded rhodochrosite crystal growth under varying solution chemistry, and (3) the competing homogeneous nucleation between rhodochrosite and Mn(II)-silicates in silica-rich solutions.

These experimental data show that homogeneous nucleation of rhodochrosite only takes place above a significantly elevated solution saturation ($\Omega \gtrsim 380$). The rate of nucleation (r_{nucl}) can be described with a generalised rate law:

$$r_{nucl}\ (\mathrm{mol\,kg^{-1}\,s^{-1}}) = 0.147 \exp\left(\frac{-83.974}{(\log \Omega_{avg})^2}\right).$$

Once nucleated, the crystal growth rate (r_{grw}; BET-surface area normalised) can be delineated as a function of solution chemistry ($1 < \Omega < 380$), following a rate law that reflects a mixed diffusion- (1st order) and surface reaction-controlled (2nd order) growth mechanism:

$$r_{grw}\ (\mathrm{mol\,kg^{-1}\,s^{-1}}) = 10^{-11.684}(\Omega_{avg} - 1)^{1.420},$$

with $R^2 = 0.91$. At comparable over-saturations, the growth rate of rhodochrosite is about 10 times faster than that of siderite ($FeCO_3$), but 6 orders of magnitude slower than that of calcite ($CaCO_3$). Despite their similar growth kinetics, far-from-equilibrium rhodochrosite growth results in a negligible kinetic C isotope effect ($\Delta^{13}C$ less than −1.27‰) in contrast to siderite, which has been shown to exhibit significant kinetic isotope fractionation. This discrepancy is attributed to extensive dissolution and re-precipitation during rhodochrosite growth, which homogenises the isotopic composition of the precipitate and that of the parent solution. Competing nucleation experiments between Mn(II)-carbonate and -silicate in silica-rich solution ($[SiO_2(aq)] = 1.25\ \mathrm{mmol\,kg^{-1}}$) demonstrated that, contrary to the Fe(II)-silicate system, Mn(II)-silicates do not precipitate under conditions relevant to surface waters on early Earth. Together, these laboratory observations imply that Mn(II)-bearing solid phases were unlikely to limit aqueous Mn(II) concentrations in anoxic aquatic systems on early Earth, and suggest that the most important removal pathways involved redox transformations and/or incorporation into Ca-bearing carbonate minerals.

1. Introduction

Manganese (Mn) is a significant constituent in the Earth's continental crust and is primarily found as divalent Mn(II) in various igneous minerals, where it substitutes for divalent iron (Fe(II)) (Post, 1999). The Precambrian sedimentary record of Mn deposition is characterised by two major episodes coinciding with the rise of free $O_2(g)$ in surface waters (ca. 2.3 Ga Great Oxygenation Event) and the later ventilation/oxygenation of deep oceans (ca. 0.7 Ga) (see reviews by Roy, 2006;

* Corresponding author.
E-mail address: zj259@cam.ac.uk (C.Z. Jiang).

https://doi.org/10.1016/j.gca.2025.12.002
Received 18 July 2025; Accepted 1 December 2025
Available online 3 December 2025

Kuleshov, 2011b; Maynard, 2010; Johnson et al., 2016). The largest sedimentary Mn deposits are found in ca. 2.2 Ga Kalahari Manganese Field, South Africa, with estimated Mn resources surpassing 13 billion tonnes, constituting over half of known Mn resources in the lithosphere (Gutzmer and Beukes, 1996; Kuleshov, 2011b; Laznicka, 1992).

Mass sedimentary Mn accumulations are thought to be initiated by oxidation of soluble Mn^{2+} into insoluble Mn(III)/(IV), which in turn, gave rise to diverse Mn mineral assemblages during diagenesis and metamorphism (e.g., Kuleshov, 2011a; Tsikos et al., 2003; Gutzmer and Beukes, 1997; Johnson et al., 2016; Mhlanga et al., 2023). This depositional model, paired with the unparallelled volume of Mn accumulation associated with the Kalahari Manganese Field, implies the existence of chemical and sedimentary processes that sustained a relatively large Mn^{2+} reservoir held in seawater prior to the rise of $O_2(g)$.

Understanding the availability of Mn^{2+} on ancient Earth is crucial in advancing our knowledge of what roles Mn^{2+} played in the origin and early evolution of life. For example, recent experiments have shown Mn^{2+} to be 10 times more effective than Mg^{2+} in catalysing prebiotically plausible, non-enzymatic ribonucleic acid (RNA) ligation reactions (Liu et al., 2024). Moreover, Mn^{2+} shaped the key stages in the co-evolution of life and its environment, exemplified by the Mn_4CaO_5 cluster at the active site of photosystem II, where the Mn cycles through oxidation states to use water as an electron source and ultimately generates $O_2(g)$ (e.g., Umena et al., 2011; Lingappa et al., 2019). This biological utilisation of Mn culminated in the Great Oxygenation Event that potentially stripped surface waters of major redox metals, including Mn^{2+}. What geochemical processes, then, regulated Mn^{2+} levels before biological intervention?

It has been hypothesised that Mn^{2+} concentrations in anoxic water bodies could have accumulated until the precipitation of Mn(II)-rich carbonate minerals, including rhodochrosite ($MnCO_3$), Mn-calcite ($CaCO_3$), and Mn-dolomite ($CaMg(CO_3)_2$) (e.g., Kuleshov, 2011b; Roy, 2006; Anbar and Holland, 1992; Crerar et al., 1980; Fischer et al., 2016; Mucci, 1988). This inference is formulated on:

1. An estimated higher heat flow from the mantle (2 to 3 times higher than the modern; Bickle, 1978; Turcotte, 1980), which would have been accompanied by more intense high-temperature hydrothermal activity that provided larger influxes of Mn(II) and Fe(II) to the early oceans (e.g., Roy, 2000; Holland, 2002; Derry and Jacobsen, 1990; Crerar, 1980; Seyfried and Janecky, 1985).
2. The lower luminosity of a young Sun, which necessitates elevated atmospheric concentrations greenhouse gases, namely CO_2, to maintain a surface temperature above freezing (the Faint Young Sun paradox; Sagan and Mullen, 1972; Kasting, 1993).

In support of the hypothesis of elevated Mn(II) concentrations preceding the rise of oxygen, geochemical analyses of Archaean Ca-carbonates consistently document 2–6 mol.% Mn(II) incorporation, orders of magnitude higher than values found in post-Archaean carbonates (Lingappa et al., 2019, and references therein). These findings have led to suggestions of plausible Mn^{2+} concentrations between 5 and 120 $\mu mol\,kg^{-1}$ in ambient Archaean seawater (Fischer et al., 2016; Mucci, 1988), similar to concentrations controlled by rhodochrosite solubility. However, field studies on anoxic natural waters frequently report significantly higher Mn^{2+} and Fe^{2+} concentrations than thermodynamic predictions (e.g., Holdren and Bricker, 1977; Jensen et al., 2002; Krylov et al., 2018; Postma, 1982), indicating that the precipitation of their respective carbonate minerals is complicated by kinetic factors.

Recent experimental investigations have characterised the sluggish precipitation of siderite ($FeCO_3$), a mineral that is isostructural (rhombohedral) with rhodochrosite and shares a near-identical solubility (Luo and Millero, 2003; Singer and Stumm, 1970). More specifically, studies have found:

1. The homogeneous nucleation (directly from the water column) of siderite requires more than 600 times supersaturation with respect to its solubility (Jiang and Tosca, 2019), and involves the formation of an amorphous precursor phase (Sel et al., 2012; Dideriksen et al., 2015).
2. Once nucleated, the extremely slow growth rate of siderite (Jiang and Tosca, 2020), 7 orders of magnitude slower than that of calcite, is unable to balance out influxes of Fe^{2+}, thereby, resulting in the sustained supersaturation often reported from anoxic natural waters.

On the basis of these considerations, it is reasonable to predict that rhodochrosite mineralisation may be subject to the same kinetic factors. If so, these kinetic influences may strongly control the concentrations at which Mn^{2+} can accumulate in anoxic waters.

Furthermore, a long-standing puzzle for geochemists studying ancient marine sediments is the consistently, slightly negative $\delta^{13}C$ values (−5 to −15‰) reported from Fe- and Mn-carbonates, compared to the near 0‰ values found in the contemporary limestone. Some scholars have proposed that these carbonates were primary precipitates from hydrothermally influenced seawater that captured the ^{13}C-depleted mantle signal (~ −6.5‰; Klein and Beukes, 1989; Kaufman et al., 1990; Beukes et al., 1990; Shanks, 2001). Others have favoured an early diagenetic origin of these carbonates from pore-water influenced by partial oxidation of organic carbon (< −25‰) coupled with microbial Fe^{3+} and $Mn^{3+/4+}$ reduction (e.g., Konhauser et al., 2005, 2017; Fischer et al., 2009; Heimann et al., 2010; Johnson et al., 2013; Mhlanga et al., 2023; Smith et al., 2023). Though the later interpretation has been more prevalent, it is challenged by the virtual absence of organic carbon in these formations (see compilation by Lotem et al., 2025; Thompson et al., 2019). Notably, the range of $\delta^{13}C$ values reported from ancient Fe- and Mn-carbonates have not, to date, captured end-member $\delta^{13}C$ values, either closer to 0‰ or below −25‰, predicted by this hypothesis (Tsikos et al., 2022; Jiang et al., 2022). To reconcile these observations, Jiang et al. (2022) experimentally demonstrated that siderite-$\delta^{13}C$ values down to −14‰ can be, in fact, achieved by abiotic, far-from-equilibrium crystal growth from a parent solution with $\delta^{13}C \simeq 0$‰. Given geochemical similarities between Fe- and Mn-carbonates discussed above, analogous kinetic C isotope effects might also be expected to accompany Mn(II)-carbonate found in ancient rocks.

Another important feature of surface water on early Earth is elevated silica ($SiO_2(aq)$) concentration, primarily governed by opal-CT (Cristobalite-Tridymite) precipitation during early diagenesis (Siever, 1992; Maliva et al., 2005). While low-temperature Mn(II)-silicates, such as bementite ($Mn_8Si_6O_{15}(OH)_{10}$) and neotocite ($(Mn,Fe)SiO_3 \cdot H_2O$), have not been unequivocally identified as primary phases in sedimentary rock (Roy, 2006; Kuleshov, 2011b), this does not preclude the potential significance of authigenic Mn(II)-silicates precipitation as transient Mn^{2+} sinks.

This study sets out to experimentally investigate (1) the requisite solution chemistry for homogeneous nucleation of Mn(II)-carbonate and -silicate, (2) the crystal growth kinetics of Mn(II) minerals as a function of solution chemistry, (3) the kinetic isotope effect associated with far-from-equilibrium crystal growth.

2. Materials and methods

2.1. Working solution preparation

Closed-system mineral syntheses were carried out at 298.15 K within a strictly anoxic Coy polymer glovebox filled with 5% H_2/95% N_2 gas and maintained at anoxic conditions by a pair of palladium catalysts and anhydrous $CaSO_4$ desiccants. The palladium catalysts scrub $O_2(g)$ in the glovebox by continuously reacting trace $O_2(g)$ with $H_2(g)$ to form $H_2O(l)$, and subsequently removed by $CaSO_4$ desiccants. The O_2 and H_2 contents in the glovebox were continuously monitored

Table 1
Initial solution chemistry of rhodochrosite nucleation (R series), in the presence of dissolved silica (RS series), and seeded crystal growth experiments (RG series). The initial chemical conditions (at t = 0 s) are denoted with (0), to be differentiated from subsequent measurements. [Mn(II)](0) and DIC(0) are calculated from added stock solutions. The initial solution saturation (Ω(0)) with respect to rhodochrosite is calculated against solubility $K_{sp} = 10^{-10.3}$ (Luo and Millero, 2003) using $\dot{B}$ equation (Helgeson et al., 1981) for estimating ionic activity coefficient, assuming no ionic speciation (Supplementary Section S1). The resulting mineralogy was characterised using XRD (Fig. 2A), FT-IR (Fig. 2B), and SEM-EDS. Solids collected from all precipitated experiments were pure rhodochrosite (*rds*), "–" indicates no precipitate was observed.

Ex.No	Initial Solution Chemistry						Resulting mineralogy
	pH	Solution Weight kg ×10³	[Mn(II)](0) mol kg⁻¹ ×10³	DIC(0) mol kg⁻¹ ×10³	logpCO_2(0) bar	Ω(0)	
R-1	6.983	616.58	1.006	7.510	−1.46	19	–
R-2	7.502	618.63	1.002	5.349	−2.07	50	–
R-3	7.252	621.27	0.998	39.279	−0.97	197	–
R-4	7.552	604.24	0.988	26.480	−1.43	275	–
R-5	7.660	612.02	0.987	23.660	−1.58	318	–
R-6	7.880	607.11	0.987	14.199	−2.02	320	–
R-7	7.990	619.23	0.987	13.072	−2.16	381	*rds*
R-8	7.752	618.22	1.003	29.248	−1.58	497	*rds*
R-9	7.535	620.47	0.988	53.297	−1.11	531	*rds*
R-10	8.124	617.63	0.989	19.620	−2.12	782	*rds*
R-11	7.791	611.67	0.987	42.945	−1.45	787	*rds*
R-12	7.640	620.59	0.988	71.009	−1.08	910	*rds*
R-13	7.751	617.00	1.005	58.438	−1.27	992	*rds*
R-14	8.249	616.01	1.006	36.657	−1.97	1979	*rds*
RS-1	7.000	615.12	0.984	2.136	−2.02	6	–
RS-2	7.500	614.69	0.984	6.068	−2.02	55	–
RS-3	07.503	609.35	0.986	19.267	−1.52	178	–
RS-4	7.753	616.19	0.979	18.739	−1.77	311	–
RS-5	7.747	611.72	0.980	33.349	−1.51	547	*rds*
RS-6	8.000	610.43	0.991	18.605	−2.02	558	*rds*
RS-7	8.059	614.25	0.979	33.044	−1.83	1122	*rds*
RS-8	8.252	612.35	0.988	33.408	−2.01	1783	*rds*
RG-1	7.250	614.71	0.986	3.558	−2.02	18	*rds*
RG-2	7.511	615.33	0.985	3.839	−2.23	36	*rds*
RG-3	7.749	613.82	0.986	4.218	−2.41	70	*rds*
RG-4	7.300	608.71	0.986	22.221	−1.27	124	*rds*
RG-5	7.505	613.74	0.986	19.228	−1.52	178	*rds*
RG-6	7.751	607.82	0.987	16.788	−1.82	280	*rds*

Ionic strength I = 0.1 mol kg⁻¹, T = 298.15 K, and 1 bar.

with a Coy CAM-12 gas analyser to ensure an atmosphere of < 1 ppm O_2 throughout the preparation and storage of stock solutions and samples.

All stock and working solutions were prepared using de-ionised water (resistivity 18.2 MΩ cm) that was first deoxygenated by purging with O_2-free N_2 gas for at least 1 h (Butler et al., 1994), then placed on a stir plate for 24 h in the glovebox to allow the residual O_2 to escape and be removed by the catalysts. $MnCl_2$ and Na_2SiO_3 stock solutions (0.5 mol kg⁻¹) were prepared by dissolving analytical grade powders (≥ 99%, Sigma-Aldrich) in the deoxygenated de-ionised water and left to homogenise for 48 h. Na_2SiO_3 stock solution was stirred at 80 °C to overcome its slow dissolution kinetics at ambient temperature. $NaHCO_3$ stock solutions (0.1 mol kg⁻¹; powder ≥ 99.7%; Sigma-Aldrich) were freshly prepared for each batch of experiments to ensure that the total dissolved inorganic carbon (DIC) across experiments was not affected by the degassing of the stock solution over time. The stoichiometric ionic strength (I = 0.1 mol kg⁻¹) of all experiments was balanced by adding predetermined amounts of NaCl.

Before being transferred into the glovebox, each borosilicate reaction vessel containing a stir bar was first filled up with de-ionised water to determine its maximum volume/weight (≃ 600 mL or g), based on which, the amounts of reagents and stock solutions were prepared. The weight of all added reagents and stock solutions was taken into account in the final calculation of the total solution weight (Table 1). This procedure serves three purposes: (1) An accurate determination of the initial solution chemistry (mol kg⁻¹). (2) To facilitate syringe-solution sampling through gas-tight septum caps. (3) To ensure the accuracy of mass-balance calculation of precipitation kinetics.

The pH conditions of all working solutions were held constant by a combination of 0.05 mol kg⁻¹ MOPS (3-(N-morpholino) propanesulfonic acid) pH buffer and large DIC pools (up to 71 mmol kg⁻¹). MOPS features significant steric hindrance of acid–base functional groups and therefore exhibits negligible metal complexation (Kandegedara and Rorabacher, 1999). Terminal pH measurement shows pH changes < 0.1 unit throughout the synthesis. Ionic strength contribution from MOPS was taken into account in ionic strength balancing (Supplementary Material Section S1).

NaCl, MOPS, and pre-determined amounts of Na_2SiO_3 stock solution were first dissolved in 400 mL deoxygenated de-ionised water in the reaction vessel, followed by pH adjustment (0.5 mol kg⁻¹ NaOH) to be within 0.5 unit of the target values and left to homogenise for 24 h. Predetermined amounts of $NaHCO_3$ stock solution were added to the homogenised working solutions, followed by fine adjustments of pH using a *in-situ* Metrohm 902 Titrando autotitrator. This procedure aims to minimise changes in carbonate speciation associated with pH adjustment. By this stage, the working solutions were ready for the addition of cation solution and seeds which initiated mineral synthesis.

2.2. Experimental design

Three sets of experiments were conducted in this study to investigate (1) the requisite chemical condition for homogeneous nucleation of rhodochrosite (R series), (2) Seeded crystal growth kinetics of rhodochrosite as a function of solution chemistry (RG series), and (3) the potential competing nucleation between Mn(II)-carbonate and Mn(II)-silicate in solution with elevated silica ($SiO_2(aq)$) concentrations (RS series).

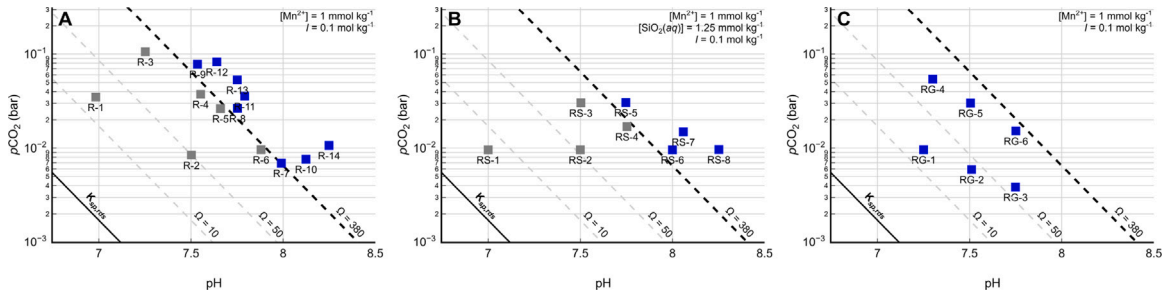

Fig. 1. pCO_2-pH plots of the starting conditions of closed-system (**A**) rhodochrosite nucleation (R series), (**B**) rhodochrosite nucleation in the presence of dissolved silica (RS series), and (**C**) rhodochrosite crystal growth experiments (RG series). Solid black lines denotes rhodochroshite solubility ($K_{sp} = 10^{-10.3}$; Luo and Millero, 2003). Dashed lines indicate the requisite supersaturation ($\Omega \simeq 380$) for homogeneous rhodochrosite nucleation (R & RS series), below which no precipitation was observed within 15 days. Seeded crystal growth experiments (RG) were designed to cover a range of solution saturation up to the nucleation threshold, where the evolution in solution chemistry is attributed to crystal growth mechanisms.

All experiments were designed to cover a wide range of solution saturations (Ω) with respect to rhodochrosite for the following reaction:

$$MnCO_3 \overset{K_{sp}}{\rightleftharpoons} Mn^{2+} + {CO_3}^{2-}, \tag{1}$$

and

$$\Omega = \frac{IAP}{K_{sp}} = \frac{\gamma_{Mn^{2+}}[Mn^{2+}]\gamma_{{CO_3}^{2-}}[{CO_3}^{2-}]}{K_{sp}}, \tag{2}$$

where $K_{sp} = 10^{-10.3}$ (Luo and Millero, 2003) is the solubility of rhodochrosite, IAP is the ionic activity product of the constituent ions in the solution, equates to their concentrations ([ ]) modified by the activity coefficient (γ); see Supplementary Material Section S1 for detailed calculations. The starting chemical conditions of all experiments are presented in Fig. 1 and Table 1.

After establishing the starting conditions of the working solutions, nucleation experiments (R and RS series) were initiated by the addition of pre-diluted (down to 0.05 $mol\,kg^{-1}$) $MnCl_2$ stock solution, in order to minimise contact nucleation upon entry of the otherwise concentrated stock solution. The working solutions were immediately topped up with de-ionised water to a maximum volume of $\simeq$ 600 mL, sealed with gas-tight septum caps that facilitate solution sampling, and gently shaken. The head-space in reaction vessels was essentially eliminated (< 1 mL) in order to minimise $CO_2(g)$ degassing over mineral syntheses. The concentrations of all reagents were re-calculated based on the final weights of the solutions.

Rhodochrosite crystal growth experiments (RG series) were designed to constrain the growth rate as a function of Ω within the range between rhodochrosite solubility and the homogeneous nucleation threshold (delineated from the nucleation experiments; Section 3.2). In total, 6 experiments were designed to cover the Ω range from 18 to 280 (Fig. 1). Unlike the nucleation experiments, $MnCl_2$ and $NaHCO_3$ stock solutions were added to the pH-buffered, homogenised working solution and left for 24 h. After visually confirming no nucleation had taken place, 0.500 g of synthetic rhodochrosite seed was added to each vessel to initiate seeded crystal growth that lasted 15 days. Rhodochrosite seed materials were prepared by mixing concentrated reagents (0.1 $mol\,kg^{-1}$) in near-neutral solutions.

2.3. Sampling and analytical methods

After establishing the initial solution chemistry, 10 time-series solution samples ($\sim$ 0.5 mL each) were extracted from each experiment through the septum caps and syringe-filtered (0.22 μm) into 10 mL 5 vol.% HNO_3 for in-house Inductively Coupled Plasma Optical Emission Spectroscopy (ICP-OES) analysis. 5 vol.% HNO_3 stabilised the diluted Mn(II) and allowed accurate dilution factor calculation by utilising a precision balance outside of the glovebox. All stock solutions were analysed with the same procedure to calibrate the initial solution chemistry. At the termination of experiments, the final pH measurements were taken and the precipitates were filtered through 0.22 μm membranes and left to dry in the low-humidity glovebox for < 24 h. Dried solids were gently homogenised using an agate mortar and pestle, then securely stored in an evacuated desiccator for *ex-situ* analyses.

Powder X-ray diffraction (XRD) characterisation was carried out on an in-house Panalytical Empyrean with Co Kα source (1.78901 Å) operated at 45.0 kV and 40.0 mA, scanned between 2 to 80 deg 2Θ at a step size of 0.013 deg and a total scan time of $\sim$ 24 min. Trial experiments demonstrated that rhodochrosite is resistant to oxidation under the ambient atmosphere for the duration of XRD analysis.

Attenuated Total Reflectance Fourier Transform Infra-red (ATR-FTIR) spectroscopy analyses were performed on powder products using a Thermo Scientific Nicolet iS5 FTIR spectrometer (Material Sciences, University of Cambridge) equipped with an iD7 Attenuated Total Reflectance (ATR) module (diamond crystal). FTIR transmission (%) was acquired for wavenumber 525 to 4000 cm^{-1} within 5 min of exposure to air. This ATR-FTIR method allows immediate and direct measurement of small amounts of solid materials and excels at distinguishing IR absorption peaks corresponding to ${CO_3}^{2-}$ versus Si–O vibration bands (e.g., Jiang and Tosca, 2019, and Fig. 4 therein).

In-house scanning electron microscopy (SEM) was performed on all precipitates to characterise their morphologies. Imaging was conducted using FEI Quanta 650 FEG SEM in high-vacuum mode. To minimise oxidation during sample preparation, small aliquots of solids were mounted on adhesive carbon layers on Al stubs within the glovebox, and were transported to a carbon-coating unit in a parafilm-sealed container. Once carbon-coated (10 nm), samples were immediately transferred into the evacuated SEM chamber.

In-house C isotope analyses were performed at the Godwin Laboratory for Palaeoclimate Research. Approximately 120 to 170 μg of the dried, homogenised sample were transferred into exetainer vials and sealed with silicone rubber septa using a screw cap. The samples were flushed with CP grade He then acidified with 104% orthophosphoric acid, left to react for 24 h at 70 °C and then analysed using a Thermo Gasbench preparation system attached to a Thermo Delta V Advantage mass spectrometer in continuous flow mode. Each run of samples was accompanied by 10 reference carbonates (Carrara Z) and 2 control samples (Fletton Clay). Carrara Z has been calibrated to VPDB using the international standard NBS19. The results are reported with reference to the international standard VPDB and the precision is better than ±0.08‰ for $^{13}C/^{12}C$.

Brunauer–Emmett–Teller (BET; Brunauer et al., 1938) surface area analysis was performed on synthetic rhodochrosite seed material and solids harvested from seeded crystal growth experiments (RG series) using 5-point N_2 sorption method (−196.828 °C) with a ChemBET 3000 surface and porosity analyser at the Department of Earth Sciences, University of Calgary.

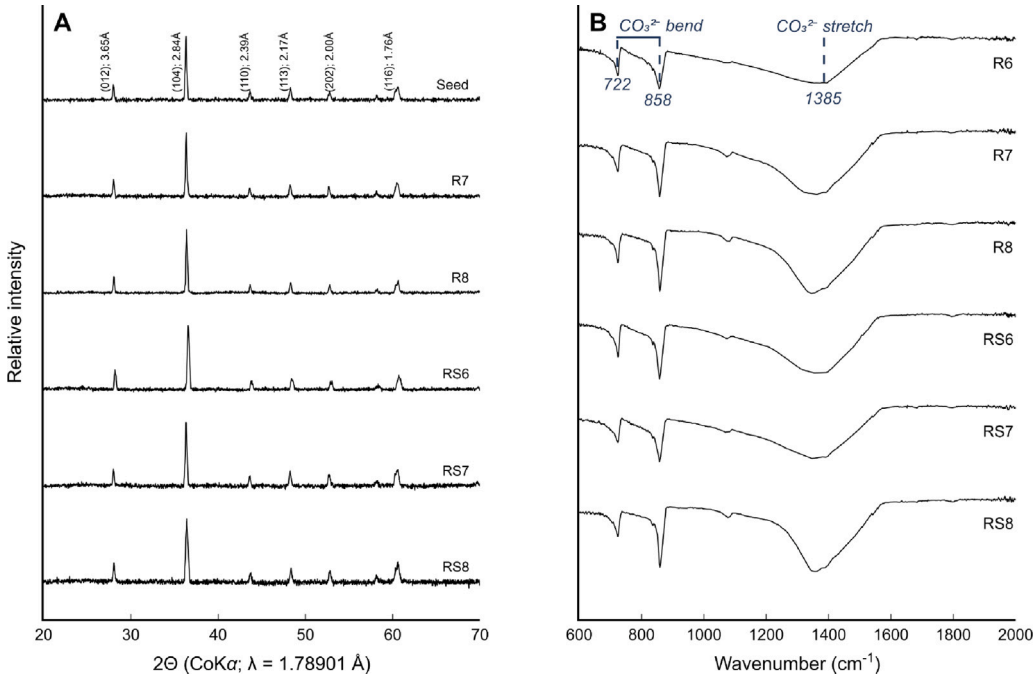

Fig. 2. (**A**) Background-removed powdered X-ray diffractograms and (**B**) ATR-FTIR spectra of selected precipitates. All precipitated experiments yielded pure rhodochrosite. XRD confirms the absence of a crystalline Mn-silicate phase, and FTIR shows no absorption peak corresponding to Si–O stretching at ~ 1030 cm^{-1}, ruling out the presence of an amorphous Mn(II)-silicate phase.

3. Results

3.1. Solid characterisation

XRD diffractograms confirm that all crystalline products are pure rhodochrosite (Fig. 2A). ATR-FTIR (transmittance mode) spectra (Fig. 2B) show absorption peaks that correspond to only CO_3^{2-} bending (722 (υ_4) and 858 (υ_2) cm^{-1}) and CO_3^{2-} stretching (1385 (υ_3) cm^{-1}). Absorption peaks corresponding to Si–O stretching (e.g., 1030 cm^{-1}) are absent in all precipitates from high-silica experiments (RS series). A combination of these two techniques signifies the absence of both a crystalline Mn(II)-silicate phase (XRD) and an amorphous Mn(II)-silicate phase (FTIR), and suggests Mn(II)-silicate does not precipitate at appreciable rates under the conditions investigated here (up to pH 8.25).

It has been noted that the wavenumber of all FTIR measurements corresponding to CO_3^{2-} stretching (1385 (υ_3) cm^{-1}) is shifted slightly from reported values (1420 (υ_3) cm^{-1}) for rhodochrosite (Fig. 2B). There could be multiple explanations behind this mismatch, however, the shift is slight and systematic, and does not hinder the differentiation between Si–O (1030 nm) and CO_3^{2-} (1385 nm) stretching, hence, not investigated further here.

SEM images show that the nucleated rhodochrosite are predominantly ~ 1 μm spherical aggregates comprised of globular-to-rhombohedral crystals that are ≃ 10 nm in edge-length (Figs. 3A & B). The narrow range of size distribution of the spherical aggregates, and the random orientation of miniature rhombi on their surface, are indicative of homogeneous nucleation of a hydrous, possibly amorphous precursor phase that started crystallising from the core outwards. These morphological features of nucleated rhodochrosite are consistent with siderite crystallised from amorphous Fe(II) carbonate precursor (Jiang and Tosca, 2019, and Fig. 5 therein).

When these nuclei were subjected to conditions favouring crystal growth (RG series) for 15 days, clear overgrowths were observed where the extent or volume of overgrowth material generally correlates with initial solution saturation (Ω(0)), from ~ 100 nm in RG-3 (Ω(0) = 70; Fig. 3C) to ~ 300 nm in RG-6 (Ω(0) = 280; Fig. 3F), whilst the particle size of the spherical aggregates remained around 1 μm. Notably, solids harvested from higher Ω(0) contained larger populations of polyhedral aggregates comprised of well-developed edge-aligned, rhombohedral crystals that are ~ 400 μm in edge length (Fig. 3 highlighted in dashed lines). These polyhedral aggregates may arise from Ostwald ripening, where the larger, more aligned crystals continued to grow at the expense of smaller, misaligned crystals; a morphological evolution towards single-crystal, rhombohedral rhodochrosite. The implications of these morphological features will be discussed together with solution chemistry evolution in the discussion Section 4.2.

BET analyses on rhodochrosite seed and solids harvested from crystal growth experiments (RG series) show inconsistent, moderate changes in surface area (between 8 to 9 $m^2\ g^{-1}$; Table. S2, Supplementary Materials), therefore, the growth rate data was normalised against their respective terminal surface area. Importantly, crystal growth caused a ~ 30% reduction in the single-point adsorption/desorption pore volume, and a ~ 45% decrease in the average pore diameter (Table. S2) in harvested solids, consistent with preferential crystal growth at active/defect sites (Lasaga, 1998c). It should be noted that, due to the lack of suitable facilities, BET analyses were performed more than one year after experiments had concluded. The extent of potential solid-state transformation and oxidation during transport cannot be ascertained here.

3.2. Solution chemistry

ICP-OES analysis reports the total dissolved Mn ($\mu g\ g^{-1}$) in a solution sample that may contain free Mn^{2+} and potential soluble Mn(II)-bearing compounds, thus, presented here as [Mn(II)]. Solid sample characterisations confirm that rhodochrosite is the only precipitate in all three sets of experiments (Fig. 2), which indicates that all changes in [Mn(II)] over time can be solely attributed to the precipitation of $MnCO_3$.

Importantly, solution chemistry revealed that a certain chemical threshold which must be surpassed for homogeneous rhodochrosite nucleation to occur: solution saturation (Ω) ≃ 380. Below this threshold,

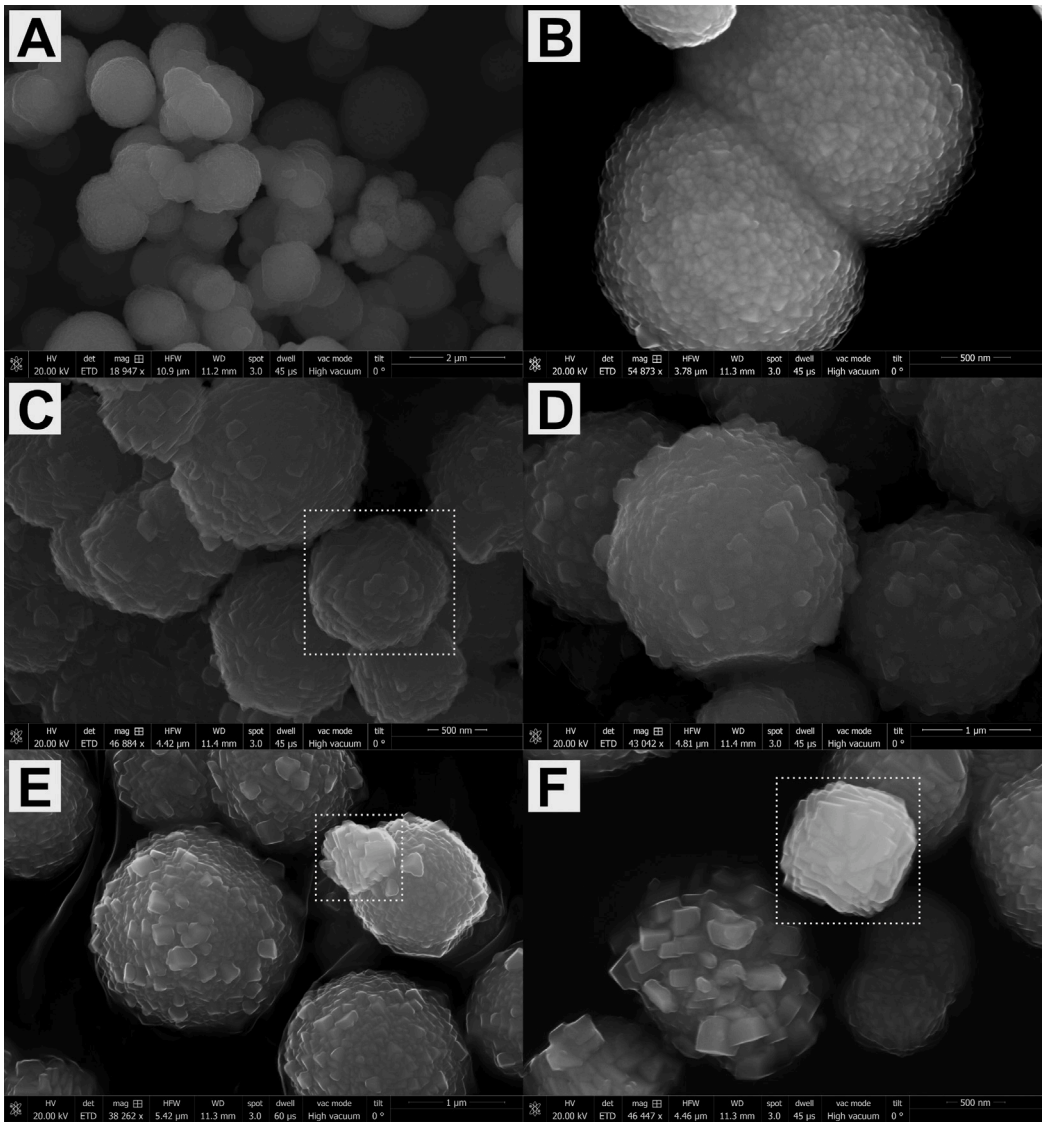

Fig. 3. SEM images of synthetic rhodochrosite seed (**A** & **B**) and solids harvested from growth experiment RG-3 to RG-6 (**C** to **F**). Nucleation experiments (R & RS series) share similar morphology as seed material: ~ 1 μm spherical aggregates of miniature rhombi that are 10s nm in edge length. After 15 days crystal growth, the extend of overgrowth of surficial rhombi qualitatively scales with initial solution saturation, up to ~ 100 nm in edge length. An increasing abundance of polyhedral aggregates comprised of ~ 400 nm, edge-aligned rhombohedral crystals are observed in high-saturation experiments (highlighted in dashed lines); reflecting a morphological maturation towards single-crystal rhodochrosite.

[Mn(II)] remained elevated and stable throughout the experimental period. Above this threshold, the rate of Mn(II) consumption increases with increasing initial solution saturation (Ω(0); Fig. 4A). The same correlation is expressed in seeded crystal growth experiments (Fig. 4B).

Given that rhodochrosite precipitation was the only sink for both Mn(II) and dissolved inorganic carbon (DIC) in all experiments, DIC evolved stoichiometrically with changes in [Mn(II)]. Assuming instantaneous carbonate speciation, the evolving Ω can be tabulated for each solution sample (Table. S3 & S4). In fact, because the rates of Mn(II) and DIC consumption correlate positively with Ω, despite the wide range in the initial composition, Ω of all growth experiments decreased to below 50 within 5 h (Fig. 5).

The nucleation of Mn(II)-silicate, however, was not observed across the parameter space investigated here; [$SiO_2(aq)$] remained constant in all RS experiments (Fig. 4D). For RS experiments initiated from Ω(0) > 380, the rate of [Mn(II)] decrease is consistent with homogeneous rhodochrosite nucleation observed in the R series (Figs. 4A & C).

3.3. C isotope analysis

The isotopic composition of precipitated ($_{pr}$) rhodochrosite (RG series) is presented in δ-notation in parts-per-thousand or ‰:

$$\delta^{13}C_{pr} = \left(\frac{^{13}R_{pr}}{^{13}R_{\mathrm{VPDB}}} - 1\right), \quad (3)$$

where $^{13}R_{pr}$ and $^{13}R_{\mathrm{VPDB}}$ are the isotopic ratio in the precipitate and Vienna Pee Dee Belemnite (0.0112372), respectively. $^{13}R_{pr}$ is calculated from a mass-balance relation between the seed and harvested solids:

$$^{13}R_{pr} = \frac{^{13}R_{solid}N_{solid} - {}^{13}R_{seed}N_{seed}}{N_{pr}}, \quad (4)$$

where N designates the mole quantities of seed material, harvested solid, and precipitated rhodochrosite, respectively; N_{seed} is converted from the mass of seed (m_{seed} = 0.500 g; N_{seed} = 4.35 mmol) and N_{pr} is stoichiometrically calculated from the total Mn(II) consumption (~ 0.7 mmol; Table 2).

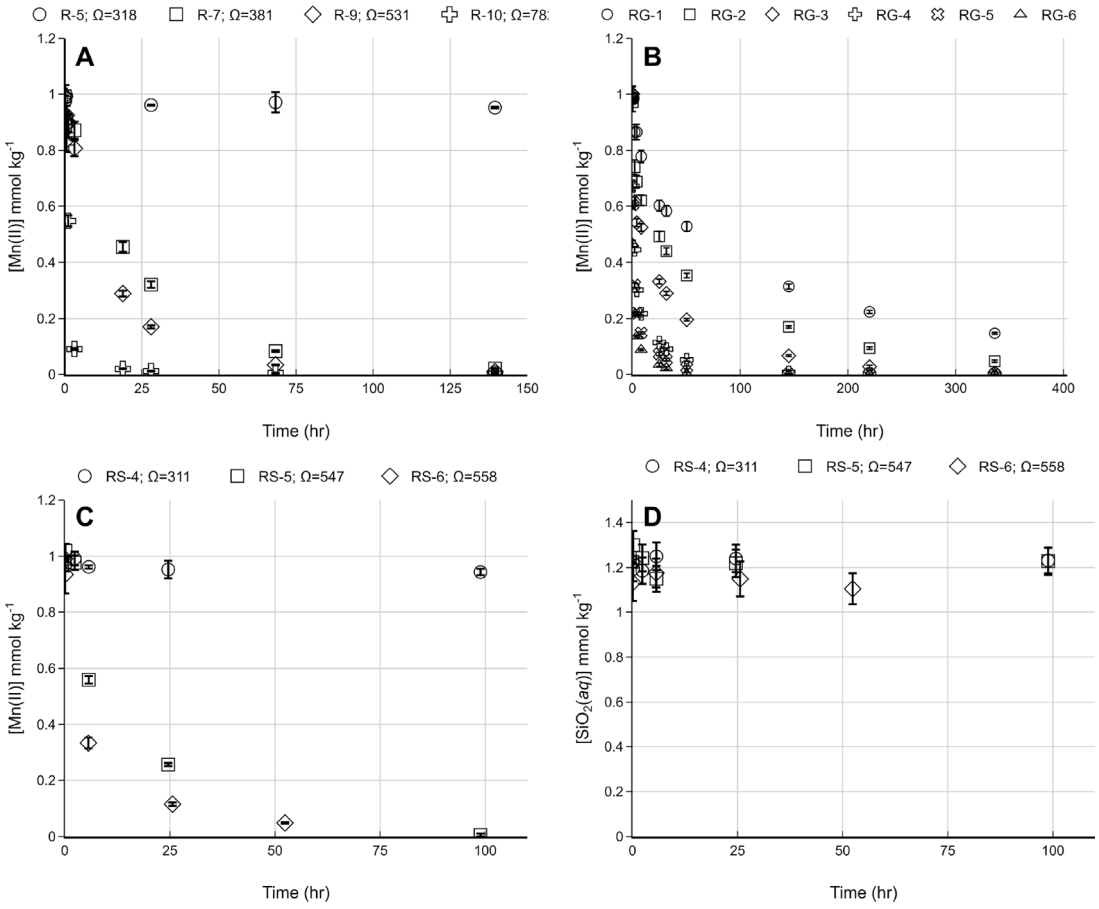

Fig. 4. Evolution of elemental concentrations over time of (**A**) rhodochrosite nucleation (R series), (**B**) crystal growth experiments (RG series), and (**C**) competing Mn(II)-carbonate-silicate nucleation (RS series). The first few days of solution chemistry with the highest sampling frequency are shown here to best differentiate among experiments. In both R and RS series, solutions with initial $\Omega < 380$ showed no drawdown of [Mn(II)] over time, indicating no nucleation took place. In solutions with initial $\Omega > 380$, the rate of Mn(II) drawdown increases with increasing Ω. In seeded rhodochrosite crystal growth experiments (RG series), the rate of [Mn(II)] drawdown increases with increasing initial Ω (i.e., RG1 → RG6), and all experiments reached near-equilibrium ($\Omega \simeq 1$) at termination. Analytical error bars are 2σ.

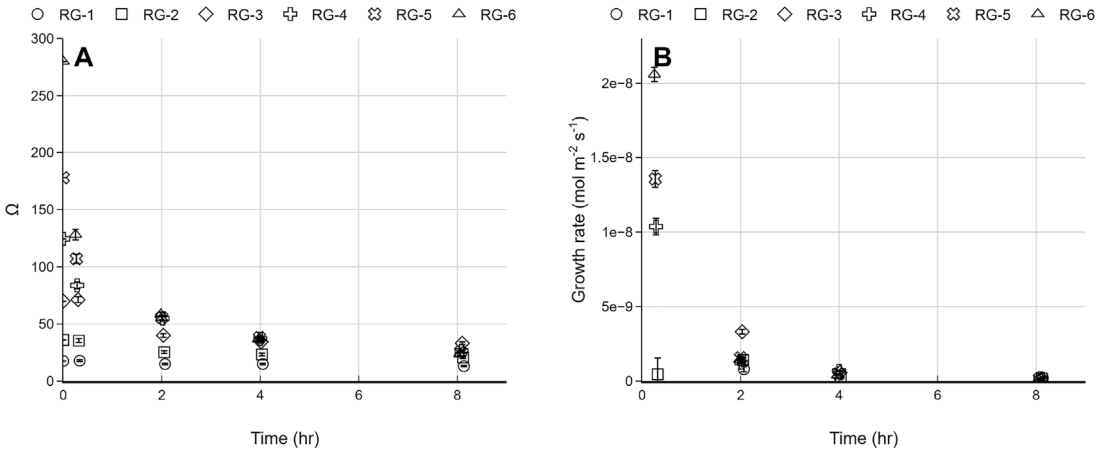

Fig. 5. Evolution of (**A**) solution saturation and (**B**) growth rate over time in closed-system, seeded rhodochrosite growth experiment (RG series). Though starting from drastically different initial solution chemistry (Ω(0) from 18 to 280), the rapid initial growth in high Ω drove all experiments to $\Omega < 50$ within 4 h, and crystal growth proceeded at $r < 1 \times 10^{-9}$ mol m^{-2} s^{-1} for the remaining period.

Table 2
C isotopic composition of precipitated rhodochrosite ($\delta^{13}C_{pr}$), seed material ($\delta^{13}C_{seed}$), and initial solution ($\delta^{13}C_{sol}$; measured from the stock $NaHCO_3$ powder). The isotopic compositions of harvested solid ($\delta^{13}C_{solid}$) and total Mn(II) precipitated (ΔMn(II)) in crystal growth experiments (RG series) allow mass-balance calculations (Eq. (4)) of the isotopic composition of precipitated rhodochrosite ($\delta^{13}C_{pr}$) and their fractionation from the initial solution ($\Delta^{13}C_{pr-sol}$). Error (1σ) for $\delta^{13}C_{pr}$ propagated from C Gasbench and elementary measurement (ICP-OES).

Ex.No	Ω(0)	$\delta^{13}C_{solid}$ ‰; 1σ	ΔMn(II) mol; 1σ ×10³	$\delta^{13}C_{pr}$ ‰; 1σ	$\Delta^{13}C_{pr-sol}$ ‰; 1σ
RG-1	18	−4.68 ± 0.08	0.614 ± 0.019	−5.05 ± 0.11	0.14 ± 0.14
RG-2	36	−4.67 ± 0.08	0.716 ± 0.019	−4.95 ± 0.11	0.24 ± 0.14
RG-3	70	−4.88 ± 0.08	0.745 ± 0.017	−6.35 ± 0.11	−1.16 ± 0.14
RG-4	124	−4.74 ± 0.08	0.664 ± 0.011	−5.47 ± 0.11	−0.28 ± 0.14
RG-5	178	−4.77 ± 0.08	0.656 ± 0.011	−5.72 ± 0.11	−0.53 ± 0.14
RG-6	280	−4.87 ± 0.08	0.652 ± 0.008	−6.46 ± 0.11	−1.27 ± 0.14
$\delta^{13}C_{seed}$					−4.63 ± 0.08
$\delta^{13}C_{sol}$					−5.19 ± 0.08

Ionic strength $I = 0.1$ mol kg^{-1}, $T = 298.15$ K, and 1 bar.

All precipitates from the growth experiments (RG series) show no significant ^{13}C depletions compared to the isotopic composition of the parent solution ($\delta^{13}C_{sol}$): $\Delta^{13}C_{pr-sol}$ ranging from -1.27 ± 0.11 to 0.24 ± 0.11‰ (Table 2). Importantly, there is no discernible correlation between $\delta^{13}C_{pr}$ and the initial solution saturation or the initial growth rate (Fig. 9).

4. Discussion

4.1. Theoretical treatment of precipitation kinetics

Nucleation and crystal growth are fundamentally distinct processes, both of which may be adequately represented by separate mathematical treatments (e.g., Lasaga, 1998a; Steefel and Van Cappellen, 1990). However, the evolution of bulk solution chemistry does not inherently distinguish between the nucleation rate and the incipient growth rate of nuclei. Consequently, rate measurements from the nucleation experiment (R series) are reported as precipitation rates (mol kg^{-1} s^{-1}; Table. S3). In contrast, seeded crystal growth experiments (RG series) were conducted below the nucleation threshold, hence, the apparent growth rate may be normalised against the terminal surface area (BET) of grown rhodochrosite (mol m^{-2} s^{-1}; Table. S4).

4.1.1. Homogeneous nucleation rate

Classical Nucleation Theory predicts a homogeneous nucleation rate (r_{nucl}) that scales exponentially with solution chemistry (e.g., Steefel and Van Cappellen, 1990; Lasaga, 1998b):

$$r_{nucl}\ (\mathrm{cm^{-3}\ s^{-1}}) = \left(\frac{2D}{d^5}\right)\exp\left(\frac{-\Delta G^*}{k_B T}\right), \tag{5}$$

where D is the diffusion constant of aqueous species (cm^2 s^{-1}), d is the effective diameter of the nuclei (cm). k_B is Boltzmann constant (J K^{-1}). ΔG^* is regarded the activation energy barrier for homogeneous nucleation of a spherical nucleus from solution, and is related to the bulk free energy change (ΔG_r) and the solution saturation (Ω) in the following:

$$\Delta G^* = \frac{16\pi\sigma^3 v^2}{3\Delta G_r{}^2} = \frac{16\pi\sigma^3 v^2}{3(k_B T \ln \Omega)^2}, \tag{6}$$

where v is the volume (cm^3) of the mineral, and σ is the solid-solution interfacial free energy (J cm^{-2}); all units above are in per unit volume. The readers are referred to Steefel and Van Cappellen (1990) and Lasaga (1998b) for detailed theoretical development. Eq. (6) states that the activation energy barrier (ΔG^*) to homogeneous nucleation decreases with increasing Ω.

By separating the saturation state and collecting unknown variables, and applying unit and logarithmic conversion, a generalised nucleation rate law can be expressed as:

$$r_{nucl}\ (\mathrm{mol\,kg^{-1}\ s^{-1}}) = k\exp\left(\frac{-b}{(\log \Omega)^2}\right), \tag{7}$$

where k is the unit-converted rate constant, and b is a factor that incorporates the surface energy and molar properties of rhodochrosite nuclei.

The exponential dependence of nucleation rate on solution saturation implies, in practice, that the initially rapid precipitation rate suffers greater time dilution due to low sampling frequency. Therefore, in delineating nucleation kinetics we consider: (1) assigning rate data to the average solution saturation (Ω_{avg}) between two sampling points, and (2) treating the measured rate data as the theoretical minimum values in curve fitting. These practices yielded a general rate law for homogeneous rhodochrosite nucleation (Fig. 6):

$$r_{nucl}\ (\mathrm{mol\,kg^{-1}\ s^{-1}}) = 0.147\exp\left(\frac{-83.974}{(\log \Omega_{avg})^2}\right). \tag{8}$$

This rate-saturation relationship reveals the kinetic factors behind the "chemical threshold" for nucleation — below this threshold, the nucleation rate is so prohibitively slow that no precipitate was observed (Figs. 1A & 4A). Therefore, this study designates the homogeneous nucleation threshold to be just below the precipitated experiment with the lowest supersaturation (R-7 $\Omega(0) = 381$). This apparent barrier to nucleation has been frequently reported from synthetic studies of sparingly soluble carbonates. For example, Sternbeck (1997) stated that rhodochrosite did not nucleate in solution with $\Omega = 500$ for at least 1 h. Similarly, Jiang and Tosca (2019) reported a requisite $\Omega \simeq 600$ for homogeneous Fe(II)-carbonate nucleation to be observed in 25 days.

It is important to note that for a natural system, the homogeneous nucleation threshold constrained here represents the upper limit for the saturation state of the corresponding mineral. In other words, in a solution with no suitable surface, a mineral saturation state could be maintained at the critical supersaturation without pervasive nucleation. Multiple other mechanisms, including the formation of a precursor phase (e.g., Montes-Hernandez and Renard, 2016; Radha and Navrotsky, 2014) and heterogeneous nucleation on suitable surfaces, can provide a lower activation energy barrier for mineralisation (Steefel and Van Cappellen, 1990; Lasaga, 1998a) and operate below the nucleation threshold delineated here. Regardless of the mechanisms, once nucleated, the kinetic behaviour of mineral-water interaction is governed by crystal growth.

4.1.2. Crystal growth rate

Kinetic data on the growth of rhodochrosite can be accurately represented with chemical affinity-based rate laws (e.g., Nancollas and Reddy, 1971; House, 1981; Aagaard and Helgeson, 1982; Lasaga, 1998c; Nielsen and Toft, 1984), which generalise growth rate (r_{grw}) as a function of energetics (Ω), and simplified into the following formalism:

$$r_{grw}\ (\mathrm{mol\,m^{-2}\ s^{-1}}) = k(\Omega - 1)^n, \tag{9}$$

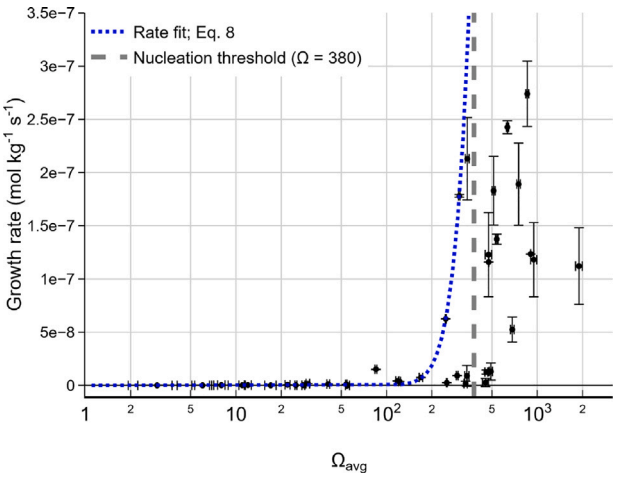

Fig. 6. Homogeneous rhodochrosite nucleation rate as a function of solution saturation, presented as precipitation rate in mol kg^{-1} s^{-1}; see Section 4.1.1 for discussion on rate law fitting. Rhodochrosite nucleation was observed only in experiments started with $\Omega > 380$ (dashed line), and the kinetic behaviour is consistent with the prediction by classic nucleation theory. All data are provided in Table. S3 (Supplementary Material). Analytical error bars are 2σ, propagated from ICP-OES measurements of [Mn(II)], and assuming $\sigma_{Mn^{2+}} = \sigma_{CO_3^{2-}}$.

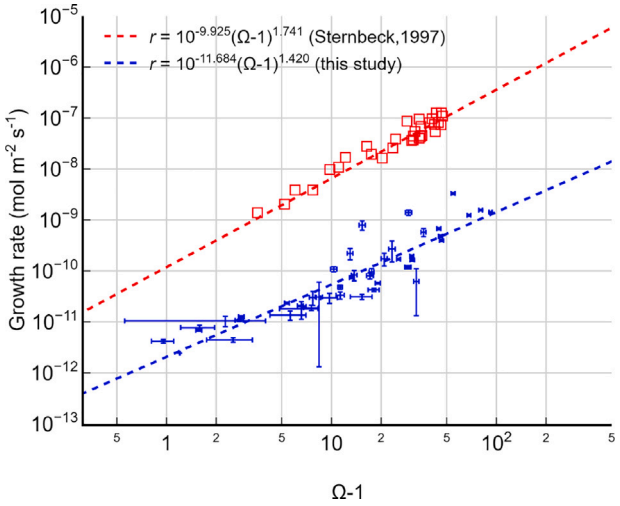

Fig. 7. BET-normalised rhodochrosite crystal growth rate (mol m^{-2} s^{-1}) as a function of solution over-saturation ($\Omega - 1$). The rate law delineated in this study (blue line) is 50 times slower than the comparable data measured by Sternbeck (1997) (solution chemistry is refitted with the same calculation scheme). Growth rates are calculated from the changes in [Mn(II)] over sampling intervals (Fig. 4B), and assigned to the average Ω between sampling points. All data are provided in Table. S4 (Supplementary Material). Analytical error bars are 2σ, propagated from ICP-OES measurements of [Mn(II)], and assuming $\sigma_{Mn^{2+}} = \sigma_{CO_3^{2-}}$.

where the exponent n is the reaction order assigned to different growth mechanisms depending on the dimensionality of reactions: $n = 1$ describes the growth rate that is controlled by adsorption or diffusion/transport processes (e.g., Nielsen, 1964; Mullin, 1972; Nielsen, 1984), $n = 2$ depicts 2-D, defect-controlled surface reactions including spiral growth and layer propagation (e.g., Nielsen, 1981; Shiraki and Brantley, 1995).

Assigning BET-surface area normalised growth rate to the evolving average solution saturation (Ω_{avg}; Table. S4), the following relationship can be established (Fig. 7):

$$r_{grw}\ (\text{mol m}^{-2}\ \text{s}^{-1}) = 10^{-11.684}(\Omega_{avg} - 1)^{1.420}, \tag{10}$$

with $R^2 = 0.91$. $n = 1.420$ implies that both surface reaction-controlled and adsorption/diffusion-controlled mechanisms operated within the range of solution chemistry investigated here ($\Omega < 280$), with the former dominating higher Ω and the latter operating near-equilibrium. Though the rate data can be further divided into two kinetic regimes that will better fit the separate growth mechanisms (as practised in Jiang and Tosca, 2020), this risks over-interpretation of the currently limited data set.

The rhodochrosite growth rate delineated here is about 50 times slower than values derived by Sternbeck (1997) (Fig. 7): r_{grw} (mol m^{-2} s^{-1}) $= 10^{-9.925}(\Omega - 1)^{1.741}$, refitted with parameters stated in the Supplementary Material section S1. This discrepancy may be attributed to the different surface properties of seed materials. More specifically, the reaction order $n = 1.741$ derived by Sternbeck (1997) indicates a more surface reaction-dominated growth mechanism (compared to $n = 1.420$ from this study), reflecting a higher abundance of surface defect sites that are not necessarily reflected in BET-surface area measurements. This is because BET-surface analysis only provides the total surface area at a roughness scale approximately the size of the adsorbing gas molecule (e.g., N_2), with no information regarding what proportion of the surface area is preferable growth sites. More specifically, the size of our synthetic seeds (~ 1 μm) is about 5 times smaller than those used by Sternbeck (1997), with a 10 times higher BET-surface area (~ 9 m^2 g^{-1}), but with a somewhat lower abundance of surface defect sites (implied by a lower reaction order n).

The lack of a reliable surface property characterisation has long plagued kinetic studies. For example, in an effort to address the dissolution rate of siderite, Golubev et al. (2009) compared different methods of surface area analysis and observed greater than 2 orders of magnitude discrepancies among commonly used methods. Before the establishment of a more comprehensive surface property characterisation method, it is concluded that the rhodochrosite growth kinetics delineated here are comparable to that reported in Sternbeck (1997).

Overlooking the potential discrepancies introduced by surface property analyses, at comparable solution chemistry, the growth rate of rhodochrosite is about 10 times faster than that of siderite (Jiang and Tosca, 2020), but is more than 6 orders of magnitude slower than that of calcite (Busenberg and Plummer, 1986; re-calculation by Jiang and Tosca, 2020) (Fig. 8). These differences in the kinetic behaviour of siderite and rhodochrosite are in broad agreement with precipitation experiments conducted by Jensen et al. (2002), where rhodochrosite-precipitating solution reached steady-state after 140 days, but siderite solution remained supersaturated for more than 474 days.

4.2. Kinetic C isotope effect in rhodochrosite crystal growth

Far-from-equilibrium crystal growth is expected to generate a discernible kinetic isotope effect (KIE) expressed by the isotopic ratio in the precipitate (R_{pr}) relative to that of the parent solution (R_{sol}), defined as the fractionation factor of a precipitating reaction (α_r). In steady-state ($_{ss}$; i.e., at a given growth rate), α_r is formulated as a logistic function of forward fractionation factor (α_f), equilibrium fractionation function (α_{eq}), net growth rate (r), and backward reaction rate (r_b) (see theoretical development summarised in DePaolo, 2011; Nielsen et al., 2012; Watkins et al., 2017; Jiang et al., 2022):

$$\alpha_r = \left(\frac{R_{pr}}{R_{sol}}\right)_{ss} = \frac{\alpha_f}{1 + \frac{r_b}{r+r_b}\left(\frac{\alpha_f}{\alpha_{eq}} - 1\right)}, \tag{11}$$

where the net rate r equals the difference between forward (r_f) and backward (r_b) rates: $r = r_f - r_b$. This theoretical framework, paired

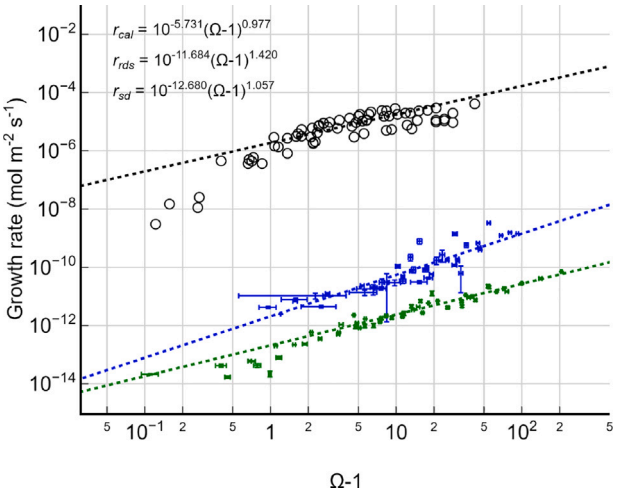

Fig. 8. BET-normalised growth rate of calcite (*cal*; open circles; Busenberg and Plummer, 1986), rhodochrosite (*rds*; blue dots), and siderite (*sd*; green dots; Jiang and Tosca, 2020) as functions of solution over-saturation ($\Omega - 1$). At a comparable over-saturation, rhodochrosite growth is about 6 orders of magnitude slower than that of calcite, but about 10 times faster than that of siderite.

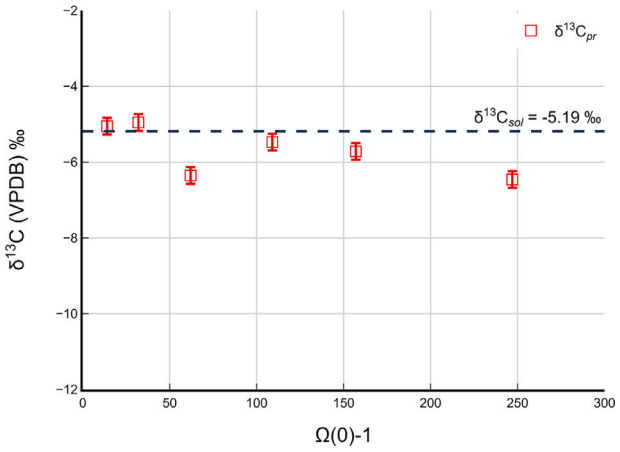

Fig. 9. C isotopic composition of precipitated rhodochrosite ($\delta^{13}C_{pr}$) from seeded crystal growth experiments (RG series) plotted against their respective initial solution saturation (Ω(0)). Dashed line indicate the starting solution C isotopic composition ($\delta^{13}C_{sol}$), measured from the stock $NaHCO_3$ powder. Despite the wide range of initial solution saturations, precipitated rhodochrosite shows no discernible kinetic C isotope effect.

with growth rate laws (Eq. (10)), allows predictions of isotopic composition in the precipitate as a function of solution chemistry. For instance, Jiang et al. (2022) implemented these relationships to explain the observed ^{13}C depletion in far-from-equilibrium siderite crystal growth, and concluded that the narrow range of $\delta^{13}C$ values (−3 to −8‰) in fine-grained (5 to 20 μm) iron formation-siderite can be explained by crystal growth from 100-time over-saturated ambient seawater (Jiang et al., 2022, and Fig. 6 therein). This abiotic, crystal growth-induced C KIE in siderite challenges the traditional view that attributes the negative $\delta^{13}C$ values to biogenic or biologically mediated processes (e.g., Heimann et al., 2010).

The nearly identical solubilities of siderite and rhodochrosite ($K_{sp,rds} = 10^{-10.3}$; Luo and Millero, 2003) and similar crystal growth kinetics (Fig. 8), might lead to the interpretation of analogous C KIE in precipitates from comparable solution conditions. However, despite an initial solution saturation (Ω(0)) up to 280, rhodochrosite crystal growth generated no discernible C KIE between the precipitate and the parent solution ($\Delta^{13}C_{pr-sol}$ less than −1.27‰; Table 2 & Fig. 9). Theoretical calculations have suggested a positive equilibrium fractionation $\Delta^{13}C_{MnCO_3-HCO_3^-;eq} = 1.6‰$ at 25 °C (Deines, 2005), which tentatively implies a potential net kinetic isotope effect of −2.87‰ in grown rhodochrosite. Nevertheless, this study did not observe a correlation between the growth rate and the kinetic isotope effect (Fig. 9), therefore, a model evaluation of the interplay between the kinetic (α_f) and the equilibrium fractionation factors (α_{eq}) during rhodochrosite growth cannot be achieved.

It is important to speculate on how α_r (Eq. (11)) may be influenced by the difference in growth kinetics (r and r_b). A comparison between the r_b values of rhodochrosite ($_{rds}$) and siderite ($_{sd}$) can be approximated to their dissolution rates in pure water, where r_f values are insignificant, hence $r \simeq -r_b$. For example, Duckworth and Martin (2003) directly observed rhodochrosite dissolution under atomic force microscope (AFM) in anoxic solution, and derived a crystal-plane normalised dissolution rate ($10^{-4.93}[H^+] + 10^{-8.45}$ mol m^{-2} s^{-1}) that is 60% faster than siderite ($10^{-8.65}$ mol m^{-2} s^{-1}) in comparable studies (Duckworth and Martin, 2004). In principle, a 60% high r_b value drives $\frac{r_b}{r+r_b} \rightarrow 1$, thus, with all other terms remaining constant, $\alpha_r \rightarrow \alpha_{eq}$. This shift, however, is countered and eclipsed by the 10 times faster rhodochrosite net growth rate (r), drives $\alpha_r \rightarrow \alpha_f$. The lack of C KIE in harvested precipitates suggests either an insignificant α_f associated with rhodochrosite growth, or other mechanisms at play.

One potential explanation for the muted C KIE might be the rapid recrystallisation of freshly grown rhodochrosite. Both rhodochrosite and siderite crystal growth followed a general morphological evolution, where growth primarily resulted in the enlargement of 10s nm miniature, surficial rhombi to 100s nm crystals (Fig. 3 compared to Jiang and Tosca, 2020, and Fig. 7 therein). However, harvested rhodochrosite from high Ω(0) experiments also featured an increasing population of polyhedral aggregates comprised of ≥ 400 nm, edge-aligned crystals (e.g., Fig. 3 highlighted in dashed lines), representing a morphological maturation towards single-crystal, rhombohedral rhodochrosite. These more matured polyhedral aggregates may reflect Ostwald ripening whereby the larger, better-developed crystals continued to grow at the expense/dissolution of the smaller (10s nm), defective and more soluble counterparts, driven by the difference in their energetic stabilities (e.g., Vengrenovitch, 1982; Kahlweit, 1965). Such a cannibalistic process is expected to be more prominent in near-equilibrium conditions where the overall growth rate is low. The inference of Ostwald ripening in far-from-equilibrium solutions may be explained by:

1. The fast initial growth in high Ω(0) solutions generated a large disparity in crystal size (hence the difference in energetic stabilities) on the surface of spherical aggregates that promotes dissolution and re-precipitation. This can be demonstrated by comparing the size range of surficial crystals in RG-5 and RG-6 (~ 50 to 100s nm; Figs. 3E&F) with the uniform size on the seeds (~ 10s nm; Figs. 3A & B).
2. The fast initial growth rapidly depleted the constituent ions in the closed-system, drastically reducing Ω towards equilibrium. In fact, despite the 18 to 280 initial Ω(0) range, all RG experiments reached Ω < 50 within 4 h (Fig. 5A). For the remaining 15 days of synthesis, rhodochrosite growth in all experiments proceeded at 1×10^{-9} mol m^{-2} s^{-1} or below (Fig. 5B); a kinetic regime where Ostwald ripening might have played a prominent role.

The recrystallisation of rhodochrosite would have homogenised the isotopic composition of freshly precipitated rhodochrosite with that in the surface fluids, thereby nullifying KIE generated by the precipitating reaction.

Although it stands to be the most approachable explanation, Ostwald ripening is expected to generate significant reductions in surface area, pore volume, and pore size in the harvested solids. This, however, is not well-supported by N_2-adsorption BET analyses (Table. S2, Supplementary Material), where the surface areas show inconsistent, moderate changes after growth, with ~ 30% reduction in the pore volume, and ~ 45% reduction in the pore size. The readers are reminded that the BET analyses were performed more than one year after the solids were harvested, due to the lack of suitable facilities. In this study, the potential solid-state transformation and oxidation during transport of the highly reactive nanocrystals/amorphous Mn carbonate precursor phase in the seed material cannot be ascertained. For example, Radha and Navrotsky (2014) demonstrated that dried, synthetic amorphous Mn carbonate crystallises into rhodochrosite in 40 days. As such, our interpretation explaining the distinct isotopic behaviours between precipitated rhodochrosite remains probationary and awaits validation through future targeted experiments.

It is worth noting that slight positive fractionations are observed in homogeneously nucleated seeds of both rhodochrosite ($\Delta^{13}C_{seed-sol}$ = +0.56‰; Table 2) and siderite ($\Delta^{13}C_{seed-sol}$ = +3.66‰; Jiang et al., 2022, and Table 1 therein). Speculatively, the classic kinetic theory suggests that homogeneous nucleation proceeds only after the fresh nuclei accumulate to a critical, thermodynamically stable size where the surface-to-volume ratio supports a precipitating flux that is larger than the dissolution flux. Before achieving this size, nuclei enriched in ^{13}C benefit from the slower kinetics of breaking the metal–$^{13}CO_3^{2-}$ bond, thereby being over-represented among stable nuclei. It is possible that the positive $\delta^{13}C$ in the nucleated seeds was carried over to the grown rhodochrosite during recrystallisation. However, such an isotopic inheritance is difficult to prove, given the muted $\Delta^{13}C_{seed-sol}$ value observed in rhodochrosite seed.

4.3. Mn^{2+} concentrations in anoxic waters

In today's oceans, soluble Mn(II) is primarily sourced from hydrothermal venting, which potentially amounts to a total Mn^{2+} influx of more than 102×10^9 mol yr^{-1}; 92% of all modelled influxes (van Hulten et al., 2017, and Table. 2 therein). These estimates are based on Mn^{2+} measurements in the west Atlantic ambient seawater (GA02 transect, GEO-TRACES programme), and upscaled proportionally to ^3He discharge from hydrothermal fluid worldwide (van Hulten et al., 2017, and references therein). In oxygenated seawater with a productive biosphere, more than 80% of hydrothermal Mn^{2+} was found to deposit as oxides and organo-aggregates within several hundred kilometres of the ridge crest (Lavelle et al., 1992). In the oxygen-deficient early Earth hydrosphere, Mn^{2+} levels are believed to have been controlled by rhodochrosite and Mn(II)-rich Ca-carbonates (Anbar and Holland, 1992; Crerar et al., 1980; Fischer et al., 2016; Mucci, 1988).

Our laboratory observations demonstrate that, in the absence of a suitable growth surface, rhodochrosite mineralisation can only proceed through homogeneous nucleation, which requires a solution chemistry that is 380 times above its solubility. This nucleation threshold implies that [Mn^{2+}] could have accumulated, at least transiently, up to mmol kg^{-1} in near-neutral, anoxic natural waters on early Earth (Fig. 10). Exceeding this threshold, however, results in an exponential increase in nucleation rate that rapidly decreases the solution saturation, that is, by depleting the constituent ions and potentially decreasing the pH. This threshold (Ω = 380), therefore, defines the maximum [Mn^{2+}] permissible in oxygen-free natural waters. Additional factors, including kinetic inhibitors and favourable mineral surfaces for heterogeneous/surface nucleation, could have further modified this threshold and warrant future investigation.

In the presence of rhodochrosite seeds, Mn^{2+} availability is subject to a crystal growth rate that is linear-to-parabolic to solution saturation (Eq. (10)). The slow, near-equilibrium growth rate of rhodochrosite implies that any influxes of Mn^{2+} will likely accumulate in solution,

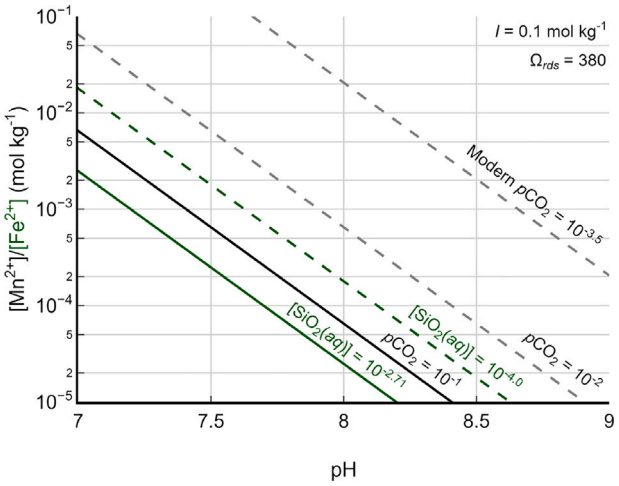

Fig. 10. Availability of Mn^{2+} and Fe^{2+} controlled by their respective nucleation thresholds for rhodochrosite (Ω = 380; black lines) and amorphous Fe(II) silicate ($IAP_{AFS} = 10^{27.6}$; green lines; Tosca et al., 2016). A lower pCO_2 leads to a higher [Mn^{2+}] that can be stable in anoxic water bodies (dashed black lines), whereas the [Fe^{2+}] is controlled by [$SiO_2(aq)$] between quartz solubility ($10^{-4.0}$; Walther and Helgeson, 1977) and amorphous silica saturation ($10^{-2.71}$; Gunnarsson and Arnórsson, 2000). Overall, given the apparent difficulty in nucleating Mn(II)-silicates, Mn^{2+} concentrations in $SiO_2(aq)$-rich, anoxic water bodies could surpass the that of Fe^{2+}.

driving solution saturation up to a level capable of sustaining a balanced growth rate against influxes (Eq. (10)). The sluggish growth rate accounts for the frequently noted rhodochrosite supersaturation in anoxic water bodies (e.g., Krylov et al., 2018; Jensen et al., 2002; Holdren and Bricker, 1977); similar to the commonly observed siderite supersaturation (Postma, 1982; Holdren and Bricker, 1977), given their comparable crystal growth kinetics (Fig. 8).

Another crucial component that could have governed metal availability in natural waters was silica concentration. Contrary to the Phanerozoic silica cycle where $SiO_2(aq)$ is actively scavenged by biomineralising organisms (e.g., radiolaria, diatoms, and sponges), the Precambrian silica cycle was primarily governed by opal-CT (Cristobalite-Tridymite) precipitation during early diagenesis (Siever, 1992), with a solubility higher than that of quartz (Rimstidt, 1997) but lower than that of amorphous silica (opal-A; Williams et al., 1985). Siliceous sediments associated with Precambrian iron formations, however, display abundant evidence for direct amorphous silica precipitation at or just below the sediment–water interface (Maliva et al., 2005; Stefurak et al., 2014). Therefore, it has been proposed that the fluids delivering abundant metals to Precambrian marine sediments were poised at amorphous silica saturation ($\log a_{SiO_2(aq)} = -2.95$ at 0 °C and −2.71 at 25 °C; Gunnarsson and Arnórsson, 2000). Upon mixing the metal-rich vent fluids with $SiO_2(aq)$-rich, high-pH ambient seawater, Fe^{2+} was rapidly consumed during homogeneous nucleation of the mineral greenalite ($Fe_3Si_2O_5(OH)_4$) (Tosca and Tutolo, 2023). These nm-sized, hydrous, and buoyant greenalite particles were dispersed and disseminated basin-wide and constituted the bulk of iron formation sediments (Rasmussen et al., 2016, 2017; Tosca et al., 2016; Tosca and Tutolo, 2023). Mn^{2+}, on the other hand, could have potentially entered the ambient seawater unhindered by $SiO_2(aq)$, and accumulated to levels that surpass the $SiO_2(aq)$-controlled Fe^{2+} concentrations (Fig. 10). This inference needs to be further examined by high-temperature Mn^{2+}-$SiO_2(aq)$ experiments in the future.

These laboratory observations combined, suggest that the direct precipitation of Mn(II)-carbonate and -silicate was unlikely to limit Mn^{2+} concentration in anoxic waters on early Earth; Their requisite nucleation thresholds were rarely exceeded. This inference is consistent

with the near-absence of mass Mn deposits in Archaean sedimentary rocks (e.g., Kuleshov, 2011b; Johnson et al., 2016; Roy, 2000, 2006; Maynard, 2010). Instead, the most important sink for Mn^{2+} was more likely to be incorporation into Ca-carbonate minerals. Geochemical analyses of Archaean carbonates show an average of 2 mol.% of Mn in Ca-carbonate, tailing up to 6 mol.% in some cases (Lingappa et al., 2019, and references therein); levels that are significantly higher than those found in post-Archaean carbonates ($\simeq$ 0 mol.%). Efforts in estimating ambient seawater levels based on Mn(II) incorporation have suggested a range between 5 to 120 $\mu mol\,kg^{-1}$ (Mucci, 1988; Fischer et al., 2016), though these estimates are contingent on assumptions regarding the often unknown kinetic behaviour of the host mineral at the time of deposition. This incorporation-based reconstruction is further complicated by the inverse correlation observed between Mn^{2+} uptake and calcite growth rate (Mucci, 1988), contrary to the more common, growth rate-independent uptake of Mg^{2+} and Sr^{2+} (Mucci and Morse, 1983).

Finally, Anbar and Holland (1992) experimentally demonstrated that Mn^{2+} undergoes photo-oxidation only at wavelengths $\lambda < 240$ nm (Anbar and Holland, 1992), a UV range that would be absorbed by CO_2 and H_2O in the atmosphere, thus, unlikely to affect surface waters (Crucilla et al., 2023). Notably, when present with equal molar Fe^{2+}, Mn^{2+} is not photo-oxidised but becomes incorporated into oxidised Fe^{3+} at a ratio of roughly 1:50 (Anbar and Holland, 1992). Furthermore, the authors delineated a Mn^{2+} photo-oxidation rate of 0.1 $mg\,cm^{-2}\,yr^{-1}$ within $300 < \lambda < 450$ nm, 1000 times slower than Fe^{2+} photo-oxidation, and probably a negligible Mn^{2+} sink on early Earth.

5. Conclusion

This experimental study concludes that:

1. homogeneous rhodochrosite nucleation requires a solution saturation that is at least 380 times higher than that corresponding to solubility equilibrium.
2. Rhodochrosite crystal growth rate is about 10 times faster than that of siderite (Jiang and Tosca, 2020), but 6 orders of magnitude slower than that of calcite (Busenberg and Plummer, 1986), at comparable solution saturation.
3. Far-from-equilibrium crystal growth of rhodochrosite did not induce a discernible kinetic carbon isotope effect, contrary to seeded siderite growth (Jiang et al., 2022). This might be partially explained by a higher exchange rate between the freshly precipitated rhodochrosite and the parent solution.
4. Mn(II)-silicate does not nucleate in solution up to pH 8.25, $[Mn^{2+}] = 1\ mmol\,kg^{-1}$, and $[SiO_2(aq)] = 1.25\ mmol\,kg^{-1}$, contrary to the rapid nucleation of amorphous Fe(II) silicate (Tosca et al., 2016; Jiang and Tosca, 2019).

These observations suggest that neither Mn(II)-carbonate nor -silicate could have limited Mn^{2+} concentrations in anoxic water bodies. Instead, the most important Mn^{2+} sink on early Earth was incorporation into Ca-bearing carbonates.

Altogether, Mn^{2+} in surface waters on early Earth could have been stable in concentrations much higher than previously appreciated, potentially exceeding those of Fe^{2+}. This conclusion expands our motivations in studying the role redox metals could have played in the origin and early evolution of life.

CRediT authorship contribution statement

Clancy Zhijian Jiang: Writing – original draft, Visualization, Validation, Software, Resources, Methodology, Investigation, Formal analysis, Data curation, Conceptualization. **Ziwei Liu:** Writing – review & editing. **Nicholas J. Tosca:** Writing – review & editing, Funding acquisition, Conceptualization.

Declaration of competing interest

The authors declare that they have no known competing financial interests or personal relationships that could have appeared to influence the work reported in this paper.

Acknowledgements

The authors thank Oleg Pokrovsky and an anonymous reviewer for thoughtful and constructive comments, and Prof. Encarnación Ruiz Agudo for editorial handling. The authors acknowledge support from the Leverhulme Centre for Life in the Universe, the Leverhulme Trust, under Grant RC-2021-032 to NJT. The authors thank Adnan Younis (University of Calgary) for conducting BET analysis, James Rolfe and Xi (Sean) Chen (Godwin Laboratory, University of Cambridge) for conducting carbon isotope analysis. CZJ and ZL value constructive discussions with Benjamin Tutolo (University of Calgary), Peter Methley (University of Cambridge), and Ş. Furkan Öztürk (California Institute of Technology).

Appendix A. Supplementary data

Supplementary Material includes thermodynamic calculations of solution chemistry and kinetic data from all experiments.

Supplementary material related to this article can be found online at https://doi.org/10.1016/j.gca.2025.12.002.

Data availability

All data and calculations are included in table format in the main text and supplementary material, and are available at Mendeley Data Archive https://doi.org/10.17632/87ykcvn58x.1.

References

Aagaard, P., Helgeson, H.C., 1982. Thermodynamic and kinetic constraints on reaction rates among minerals and aqueous solutions; I, Theoretical considerations. Am. J. Sci. 282 (3), 237–285.

Anbar, A.D., Holland, H.D., 1992. The photochemistry of manganese and the origin of banded iron formations. Geochim. Cosmochim. Acta 56 (7), 2595–2603.

Beukes, N.J., Klein, C., Kaufman, A.J., Hayes, J.M., 1990. Carbonate petrography, kerogen distribution, and carbon and oxygen isotope variations in an early Proterozoic transition from limestone to iron-formation deposition, Transvaal Supergroup, South Africa. Econ. Geol. 85 (4), 663–690.

Bickle, M., 1978. Heat loss from the earth: A constraint on Archaean tectonics from the relation between geothermal gradients and the rate of plate production. Earth Planet. Sci. Lett. 40 (3), 301–315.

Brunauer, S., Emmett, P.H., Teller, E., 1938. Adsorption of gases in multimolecular layers. J. Am. Chem. Soc. 60 (2), 309–319.

Busenberg, E., Plummer, L.N., 1986. A comparative study of the dissolution and crystal growth kinetics of calcite and aragonite. US Geol. Surv. Bull. 1578 (August), 139–168.

Butler, I.B., Schoonen, M.A., Rickard, D.T., 1994. Removal of dissolved oxygen from water: A comparison of four common techniques. Talanta 41 (2), 211–215.

Crerar, D.A., 1980. Geochemistry of manganese: an overview. In: Varentsov, I.M., Grasselly, G. (Eds.), In: Geology and Geochemistry of Manganese, vol. 1, E. Schweizerbart'sche Verlagsbuchhandlung, Stuttgart, pp. 293–334.

Crerar, D.A., Fischer, A.G., Plaza, C., 1980. Metallogenium and biogenic deposition of manganese from Precambrian to recent time. In: Varetsov, I., Grasselly, G. (Eds.), In: Geology and Geochemistry of Manganese, vol. 3, Akademiai Kiado, pp. 285–304.

Crucilla, S.J., Ding, D., Lozano, G.G., Szostak, J.W., Sasselov, D.D., Kufner, C.L., 2023. UV-driven self-repair of cyclobutane pyrimidine dimers in RNA. Chem. Commun. 59 (91), 13603–13606.

Deines, P., 2005. Erratum: "Carbon isotope effects in carbonate systems" (Geochimica et Cosmochimica Acta (2004) vol. 68 (2659–2679)). In: Geochimica Et Cosmochimica Acta, vol. 69, (21), Elsevier Ltd, pp. 5143–5144.

DePaolo, D.J., 2011. Surface kinetic model for isotopic and trace element fractionation during precipitation of calcite from aqueous solutions. Geochim. Cosmochim. Acta 75 (4), 1039–1056.

Derry, L.A., Jacobsen, S.B., 1990. The chemical evolution of Precambrian seawater: Evidence from REEs in banded iron formations. Geochim. Cosmochim. Acta 54 (11), 2965–2977.
Dideriksen, K., Frandsen, C., Bovet, N., Wallace, A.F., Sel, O., Arbour, T., Navrotsky, A., De Yoreo, J.J., Banfield, J.F., 2015. Formation and transformation of a short range ordered iron carbonate precursor. Geochim. Cosmochim. Acta 164, 94–109.
Duckworth, O.W., Martin, S.T., 2003. Connections between surface complexation and geometric models of mineral dissolution investigated for rhodochrosite. Geochim. Cosmochim. Acta 67 (10), 1787–1801.
Duckworth, O.W., Martin, S.T., 2004. Role of molecular oxygen in the dissolution of siderite and rhodochrosite. Geochim. Cosmochim. Acta 68 (3), 607–621.
Fischer, W.W., Hemp, J., Valentine, J.S., 2016. How did life survive earth's great oxygenation? Curr. Opin. Chem. Biol. 31, 166–178.
Fischer, W.W., Schroeder, S., Lacassie, J.P., Beukes, N.J., Goldberg, T., Strauss, H., Horstmann, U.E., Schrag, D.P., Knoll, A.H., 2009. Isotopic constraints on the Late Archean carbon cycle from the Transvaal Supergroup along the western margin of the Kaapvaal Craton, South Africa. Precambrian Res. 169 (1–4), 15–27.
Golubev, S., Bénézeth, P., Schott, J., Dandurand, J., Castillo, A., 2009. Siderite dissolution kinetics in acidic aqueous solutions from 25 to 100 °C and 0 to 50 atm pCO2. Chem. Geol. 265 (1–2), 13–19.
Gunnarsson, I., Arnórsson, S., 2000. Amorphous silica solubility and the thermodynamic properties of H4SiO4° in the range of 0°to 350 °C at P(sat). Geochim. Cosmochim. Acta 64 (13), 2295–2307.
Gutzmer, J., Beukes, N.J., 1996. Mineral paragenesis of the Kalahari manganese field, South Africa. Ore Geol. Rev. 11 (6), 405–428.
Gutzmer, J., Beukes, N.J., 1997. Effects of mass transfer, compaction and secondary porosity on hydrothermal upgrading of Paleoproterozoic sedimentary manganese ore in the Kalahari manganese field, South Africa. Miner. Deposita 32 (3), 250–256.
Heimann, A., Johnson, C.M., Beard, B.L., Valley, J.W., Roden, E.E., Spicuzza, M.J., Beukes, N.J., 2010. Fe, C, and O isotope compositions of banded iron formation carbonates demonstrate a major role for dissimilatory iron reduction in 2.5Ga marine environments. Earth Planet. Sci. Lett. 294 (1–2), 8–18.
Helgeson, H.C., Kirkham, D.H., Flowers, G.C., 1981. Theoretical prediction of the thermodynamic behavior of aqueous electrolytes by high pressures and temperatures; IV, Calculation of activity coefficients, osmotic coefficients, and apparent molal and standard and relative partial molal properties to 600 °C and 5 kb. Am. J. Sci. 281 (10), 1249–1516.
Holdren, G.R., Bricker, O.P., 1977. Distribution and control of dissolved iron and manganese in the interstitial waters of the Chesapeake Bay. In: Drucker, H., Wildung, R.F. (Eds.), Biological Implications of Metals in the Environment, ERDA Symp. Ser.. Technical Information Center, Washington, pp. 178–196.
Holland, H.D., 2002. Volcanic gases, black smokers, and the great oxidation event. Geochim. Cosmochim. Acta 66 (21), 3811–3826.
House, W.A., 1981. Kinetics of crystallisation of calcite from calcium bicarbonate solutions. J. Chem. Soc. Faraday Trans. 1: Phys. Chem. Condens. Phases 77 (2), 341.
van Hulten, M., Middag, R., Dutay, J.-C., de Baar, H., Roy-Barman, M., Gehlen, M., Tagliabue, A., Sterl, A., 2017. Manganese in the west Atlantic Ocean in the context of the first global ocean circulation model of manganese. Biogeosciences 14 (5), 1123–1152.
Jensen, D.L., Boddum, J.K., Tjell, J.C., Christensen, T.H., 2002. The solubility of rhodochrosite (MnCO3) and siderite (FeCO3) in anaerobic aquatic environments. Appl. Geochem. 17 (4), 503–511.
Jiang, C.Z., Halevy, I., Tosca, N.J., 2022. Kinetic isotope effect in siderite growth: Implications for the origin of banded iron formation siderite. Geochim. Cosmochim. Acta 322, 260–273.
Jiang, C.Z., Tosca, N.J., 2019. Fe(II)-carbonate precipitation kinetics and the chemistry of anoxic ferruginous seawater. Earth Planet. Sci. Lett. 506, 231–242.
Jiang, C.Z., Tosca, N.J., 2020. Growth kinetics of siderite at 298.15 K and 1 bar. Geochim. Cosmochim. Acta 274, 97–117.
Johnson, C.M., Ludois, J.M., Beard, B.L., Beukes, N.J., Heimann, A., 2013. Iron formation carbonates: Paleoceanographic proxy or recorder of microbial diagenesis? Geology 41 (11), 1147–1150.
Johnson, J.E., Webb, S.M., Ma, C., Fischer, W.W., 2016. Manganese mineralogy and diagenesis in the sedimentary rock record. Geochim. Cosmochim. Acta 173, 210–231.
Kahlweit, M., 1965. Ageing of precipitates by ostwald ripening. Angew. Chem. Int. Ed. Engl. 4 (5), 444–445.
Kandegedara, A., Rorabacher, D.B., 1999. Noncomplexing tertiary amines as "better" buffers covering the range of pH 3-11. Temperature dependence of their acid dissociation constants. Anal. Chem. 71 (15), 3140–3144.
Kasting, J.F., 1993. Earth's early atmosphere. Science 259 (5097), 920–926.
Kaufman, A.J., Hayes, J.M., Klein, C., 1990. Primary and diagenetic controls of isotopic compositions of iron-formation carbonates. Geochim. Cosmochim. Acta 54 (12), 3461–3473.
Klein, C., Beukes, N.J., 1989. Geochemistry and sedimentology of a facies transition from limestone to iron-formation deposition in the early Proterozoic Transvaal Supergroup, South Africa. Econ. Geol. 84 (7), 1733–1774.
Konhauser, K., Newman, D.K., Kappler, A., 2005. The potential significance of microbial Fe(III) reduction during deposition of Precambrian banded iron formations. Geobiology 3 (3), 167–177.
Konhauser, K., Planavsky, N., Hardisty, D., Robbins, L., Warchola, T., Haugaard, R., Lalonde, S., Partin, C., Oonk, P., Tsikos, H., Lyons, T., Bekker, A., Johnson, C., 2017. Iron formations: A global record of Neoarchaean to Palaeoproterozoic environmental history. Earth-Sci. Rev. 172 (June), 140–177.
Krylov, A.A., Hachikubo, A., Minami, H., Pogodaeva, T.V., Zemskaya, T.I., Krzhizhanovskaya, M.G., Poort, J., Khlystov, O.M., 2018. Authigenic rhodochrosite from a gas hydrate-bearing structure in Lake Baikal. Int. J. Earth Sci. 107 (6), 2011–2022.
Kuleshov, V.N., 2011a. Manganese deposits: Communication 1. Genetic models of manganese ore formation. Lithol. Miner. Resour. 46 (5), 473–493.
Kuleshov, V.N., 2011b. Manganese deposits: Communication 2. Major epochs and phases of manganese accumulation in the Earth's history. Lithol. Miner. Resour. 46 (6), 546–565.
Lasaga, A.C., 1998a. Kinetic Theory in the Earth Sciences. Princeton University Press, Princeton, p. 811.
Lasaga, A.C., 1998b. 6.4. Nucleation rate theory. In: Holland, H.D. (Ed.), Kinetic Theory in the Earth Sciences. Princeton University Press, Princeton, pp. 520–580.
Lasaga, A.C., 1998c. 7. Theory of crystal growth and dissolution. In: Holland, H.D. (Ed.), Kinetic Theory in the Earth Sciences. Princeton University Press, Princeton, pp. 581–618.
Lavelle, J.W., Cowen, J.P., Massoth, G.J., 1992. A model for the deposition of hydrothermal manganese near ridge crests. J. Geophys. Res.: Ocean. 97 (C5), 7413–7427.
Laznicka, P., 1992. Manganese deposits in the global lithogenetic system: Quantitative approach. Ore Geol. Rev. 7 (4), 279–356.
Lingappa, U.F., Monteverde, D.R., Magyar, J.S., Valentine, J.S., Fischer, W.W., 2019. How manganese empowered life with dioxygen (and vice versa). Free Radic. Biol. Med. 140, 113–125.
Liu, Z., Jiang, C.Z., Bond, A.D., Tosca, N.J., Sutherland, J.D., 2024. Manganese(ii) promotes prebiotically plausible non-enzymatic RNA ligation reactions. Chem. Commun. 60 (51), 6528–6531.
Lotem, N., Rasmussen, B., Zi, J.-W., Zeichner, S.S., Present, T.M., Bar-On, Y.M., W. Fischer, W., 2025. Reconciling Archean organic-rich mudrocks with low primary productivity before the Great Oxygenation Event. Proc. Natl. Acad. Sci. 122 (2), 2017.
Luo, Y., Millero, F.J., 2003. Solubility of rhodochrosite (MnCO3) in NaCl solutions. J. Solut. Chem. 32 (5), 405–416.
Maliva, R.G., Knoll, A.H., Simonson, B.M., 2005. Secular change in the Precambrian silica cycle: Insights from chert petrology. Geol. Soc. Am. Bull. 117 (7), 835.
Maynard, J.B., 2010. The chemistry of manganese ores through time: A signal of increasing diversity of earth-surface environments. Econ. Geol. 105 (3), 535–552.
Mhlanga, X.R., Tsikos, H., Lee, B., Rouxel, O.J., Boyce, A.C., Harris, C., Lyons, T.W., 2023. The Palaeoproterozoic Hotazel BIF-Mn Formation as an archive of Earth's earliest oxygenation. In: Earth-Science Reviews, vol. 240, Elsevier B.V., 104389.
Montes-Hernandez, G., Renard, F., 2016. Time-resolved in situ Raman spectroscopy of the nucleation and growth of siderite, magnesite, and calcite and their precursors. Cryst. Growth & Des. 16 (12), 7218–7230.
Mucci, A., 1988. Manganese uptake during calcite precipitation from seawater: Conditions leading to the formation of a pseudokutnahorite. Geochim. Cosmochim. Acta 52 (7), 1859–1868.
Mucci, A., Morse, J.W., 1983. The incorporation of Mg2+ and Sr2+ into calcite overgrowths: influences of growth rate and solution composition. Geochim. Cosmochim. Acta 47 (2), 217–233.
Mullin, J.W., 1972. Crystallization, second ed. Butterworth, London, p. 600.
Nancollas, G.H., Reddy, M.M., 1971. The crystallization of calcium carbonate. II. Calcite growth mechanism. J. Colloid Interface Sci. 37 (4), 824–830.
Nielsen, A.E., 1964. Kinetics of Precipitation. Pergamon Press, New York.
Nielsen, A.E., 1981. Theory of electrolyte crystal growth the parabolic rate law. Pure Appl. Chem. 53 (11), 2025–2039.
Nielsen, A.E., 1984. Electrolyte crystal growth mechanisms. J. Cryst. Growth 67 (2), 289–310.
Nielsen, L.C., DePaolo, D.J., De Yoreo, J.J., 2012. Self-consistent ion-by-ion growth model for kinetic isotopic fractionation during calcite precipitation. Geochim. Cosmochim. Acta 86, 166–181.
Nielsen, A.E., Toft, J.M., 1984. Electrolyte crystal growth kinetics. J. Cryst. Growth 67 (2), 278–288.
Post, J.E., 1999. Manganese oxide minerals: Crystal structures and economic and environmental significance. Proc. Natl. Acad. Sci. USA 96 (7), 3447–3454.
Postma, D., 1982. Pyrite and siderite formation in brackish and freshwater swamp sediments. Am. J. Sci. 282 (8), 1151–1183.
Radha, A.V., Navrotsky, A., 2014. Manganese carbonate formation from amorphous and nanocrystalline precursors: Thermodynamics and geochemical relevance. Am. Mineral. 99 (5–6), 1063–1070.
Rasmussen, B., Muhling, J.R., Suvorova, A., Krapež, B., 2016. Dust to dust: Evidence for the formation of "primary" hematite dust in banded iron formations via oxidation of iron silicate nanoparticles. Precambrian Res. 284, 49–63.
Rasmussen, B., Muhling, J.R., Suvorova, A., Krapež, B., 2017. Greenalite precipitation linked to the deposition of banded iron formations downslope from a late Archean carbonate platform. Precambrian Res. 290, 49–62.

Rimstidt, J., 1997. Quartz solubility at low temperatures. Geochim. Cosmochim. Acta 61 (13), 2553–2558.
Roy, S., 2000. Late Archean initiation of manganese metallogenesis: its significance and environmental controls. Ore Geol. Rev. 17 (3), 179–198.
Roy, S., 2006. Sedimentary manganese metallogenesis in response to the evolution of the Earth system. Earth-Sci. Rev. 77 (4), 273–305.
Sagan, C., Mullen, G., 1972. Earth and mars: Evolution of atmospheres and surface temperatures. Science 177 (4043), 52–56.
Sel, O., Radha, A., Dideriksen, K., Navrotsky, A., 2012. Amorphous iron (II) carbonate: Crystallization energetics and comparison to other carbonate minerals related to CO2 sequestration. Geochim. Cosmochim. Acta 87, 61–68.
Seyfried, W., Janecky, D., 1985. Heavy metal and sulfur transport during subcritical and supercritical hydrothermal alteration of basalt: Influence of fluid pressure and basalt composition and crystallinity. Geochim. Cosmochim. Acta 49 (12), 2545–2560.
Shanks, W.C., 2001. Stable isotopes in seafloor hydrothermal systems: Vent fluids, hydrothermal deposits, hydrothermal alteration, and microbial processes. Rev. Miner. Geochem. 43 (1), 469–525.
Shiraki, R., Brantley, S.L., 1995. Kinetics of near-equilibrium calcite precipitation at 100 °C: An evaluation of elementary reaction-based and affinity-based rate laws. Geochim. Cosmochim. Acta 59 (8), 1457–1471.
Siever, R., 1992. The silica cycle in the Precambrian. Geochim. Cosmochim. Acta 56 (8), 3265–3272.
Singer, P.C., Stumm, W., 1970. The solubility of ferrous iron in carbonate-bearing waters. J. - Am. Water Work. Assoc. 62 (3), 198–202.
Smith, A.J., Beukes, N.J., Cochrane, J.M., Gutzmer, J., 2023. Manganese carbonate-bearing mudstone of the Witwatersrand-Mozaan succession in southern Africa as evidence for bacterial manganese respiration and availability of free molecular oxygen in Mesoarchaean oceans. South Afr. J. Geol. 126 (1), 29–48.
Steefel, C.I., Van Cappellen, P., 1990. A new kinetic approach to modeling water-rock interaction: The role of nucleation, precursors, and Ostwald ripening. Geochim. Cosmochim. Acta 54 (10), 2657–2677.
Stefurak, E.J., Lowe, D.R., Zentner, D., Fischer, W.W., 2014. Primary silica granules—A new mode of Paleoarchean sedimentation. Geology 42 (4), 283–286.
Sternbeck, J., 1997. Kinetics of rhodochrosite crystal growth at 25 °C: The role of surface speciation. Geochim. Cosmochim. Acta 61 (4), 785–793.
Thompson, K.J., Kenward, P.A., Bauer, K.W., Warchola, T., Gauger, T., Martinez, R., Simister, R.L., Michiels, C.C., Llirós, M., Reinhard, C.T., Kappler, A., Konhauser, K.O., Crowe, S.A., 2019. Photoferrotrophy, deposition of banded iron formations, and methane production in Archean oceans. Sci. Adv. 5 (11).
Tosca, N.J., Guggenheim, S., Pufahl, P.K., 2016. An authigenic origin for Precambrian greenalite: Implications for iron formation and the chemistry of ancient seawater. Geol. Soc. Am. Bull. 128 (3–4), 511–530.
Tosca, N.J., Tutolo, B.M., 2023. Hydrothermal vent fluid-seawater mixing and the origins of Archean iron formation. Geochim. Cosmochim. Acta 352, 51–68.
Tsikos, H., Beukes, N.J., Moore, J.M., Harris, C., 2003. Deposition, diagenesis, and secondary enrichment of metals inthe Paleoproterozoic Hotazel iron formation, Kalahari manganese field, SouthAfrica. Econ. Geol. 98 (7), 1449–1462.
Tsikos, H., Siahi, M., Rafuza, S., Mhlanga, X.R., Oonk, P.B., Papadopoulos, V., Boyce, A.J., Mason, P.R., Harris, C., Gröcke, D.R., Lyons, T.W., 2022. Carbon isotope stratigraphy of Precambrian iron formations and possible significance for the early biological pump. Gondwana Res. 109, 416–428.
Turcotte, D., 1980. On the thermal evolution of the earth. Earth Planet. Sci. Lett. 48 (1), 53–58.
Umena, Y., Kawakami, K., Shen, J.R., Kamiya, N., 2011. Crystal structure of oxygen-evolving photosystem II at a resolution of 1.9 å. Nature 473 (7345), 55–60.
Vengrenovitch, R., 1982. On the ostwald ripening theory. Acta Metall. 30 (6), 1079–1086.
Walther, J.V., Helgeson, H.C., 1977. Calculation of the thermodynamic properties of aqueous silica and the solubility of quartz and its polymorphs at high pressures and temperatures. Am. J. Sci. 277 (10), 1315–1351.
Watkins, J.M., DePaolo, D.J., Watson, E.B., 2017. Kinetic fractionation of non-traditional stable isotopes by diffusion and crystal growth reactions. Rev. Miner. Geochem. 82 (1), 85–125.
Williams, L.A., Parks, G.A., Crerar, D.A., 1985. Silica diagenesis, I. Solubility controls. SEPM J. Sediment. Res. 55.